Chromophore photoreduction in red fluorescent proteins is responsible for bleaching and phototoxicity: Supporting Information

Russell B. Vegh[a,b], Ksenia B. Bravaya[c], Dmitry A. Bloch[d], Andreas S. Bommarius[a,b,e], Laren M. Tolbert[a], Michael Verkhovsky[d] (deceased), Anna I. Krylov[c], Kyril M. Solntsev[a]

[a] School of Chemistry and Biochemistry Georgia Institute of Technology, Atlanta, Georgia 30332-0363, USA

[b] Parker H. Petit Institute of Bioengineering and Biosciences,
Georgia Institute of Technology, Atlanta, Georgia 30332-0363, USA

[c] Department of Chemistry, University of Southern California,
Los Angeles, CA 90089-0482, USA

[d] Institute of Biotechnology, University of Helsinki, Helsinki, Finland

[e] School of Chemical and Bio-molecular Engineering,
Georgia Institute of Technology, Atlanta, GA 30332, USA

I. EXPERIMENTAL DETAILS

A. Protein expression and purification

The gene encoding DsRed was amplified from DsRed2-1 plasmid (BD Biosciences Clontech, Palo Alto, CA) and cloned into pProTet (Clonetech) between *Sal*I and *Not*I restrictions sites and contained an N-terminal 6xHN affinity tag. The genes encoding KillerRed and mRFP (Genbank accession numbers AAY40168.1 and AAM54544, respectively) were cloned into pProTet between the *Sal*I and *Not*I restriction sites and contain an N-terminal 6xHN affinity tag. For protein expression, the plasmids were transformed into *E. coli* DH5-alpha-pro. A 5 mL culture was inoculated into 1 L of Lysogeny Broth (LB, pH 7) containing 35 μg/mL of chloramphenicol, grown to an OD600 of 0.4 at 35°C (2-3 h), and then induced with anhydrotetracycline (1 mg/mL). The proteins were overexpressed to 20% of cell protein and purified the protein via Ni^{2+}-nitrilotriacetic acid (NTA)-immobilized metal affinity chromatography (IMAC). All measurements were performed in phosphate buffer saline (PBS, 50 mM sodium phosphate, 250 mM NaCl, pH 7.5), unless stated otherwise.

B. Time-correlated single photon counting measurements

Time-resolved fluorescence was acquired using the Time-Correlated Single Photon Counting method (TCSPC). In these measurements, a picosecond diode laser (LDH-P-C-470, Picoquant) and sub-nanosecond LED excitation pulses (EPLED 590, Edinburgh Instruments) emitting at 467 nm and 590 nm, respectively, were used as excitation light sources. The detector was a high speed microchannel plate photomultiplier tube (Hammamatsu R3809U-50) cooled to -20°C to reduce noise. The pulses were communicated to a hardware controller by a constant fraction discriminator (CFD). A second CFD was used to obtain a timing reference pulse from the light source. The time-amplitude-converter output voltage was sent through a biased amplifier with a variable gain and a variable offset and the amplified signal was fed to the analog-to-digital converter. A multichannel analyzer software (Edinburg Instruments F900) was used to process the signal and convert it to a PC format. Fluorescence lifetime data was fit to polyexponential decay function using the program FFIT provided by professor Nikolai Tkachenko at the Tampere University of Technology (Tampere, Finland). The instrument response functions (IRF) were measured and used to deconvolute the fluorescence decay.

C. Transient absorption spectroscopy measurements (picosecond-to-nanosecond time domain)

Femtosecond transient absorption measurements were performed in Dr. Joseph Perry's lab (Georgia Tech, Atlanta). Spectra were acquired using a commercial transient absorption spectroscopy system (Newport, Helios). This system accepts two input laser beams, one of variable wavelength used as the pump beam and one of a fixed wavelength used to generate the probe beam in a proprietary nonlinear optical crystal. All experiments were performed using the TOPAS output at 532 nm with a pulse width of 100 fs. A small portion ($\sim$5%) of a Ti:Sapphire regenerative amplifier (Newport, Spitfire, 800 nm, 1 kHz, Spectra-physics) provided the probe pulse to generate the white-light continuum (WLC, 420-850 nm, 850-1650 nm). At these specifications, the instrument response function is approximately 200 fs. At each time point, data were averaged for 2 s. The Helios pump beam was chopped at 500 Hz to obtain pumped (signal) and non-pumped (reference) absorption spectra of the sample. A correction factor for chirp in the probe beam was generated using the ultrafast response of CCl_4, and was applied to all data sets. The data were stored as 3-D wavelength-time-absorbance matrices that were exported for use with the fitting

software. The protein solutions had an OD532 of ~0.5 in 2 mm path-length cuvettes, and were stirred continually throughout the data acquisition. The pump intensity was 575 mW/cm^2.

D.   Transient absorption spectroscopy measurements (μs-to-second time domain)

In the present study, a custom-built kinetic setup based on ANDOR and Basler Vision microarray imaging cameras was used, allowing the broadband TA measurements with 1 μs time resolution after a single pulse excitation. This setup, previously used to study multiheme O$_2$-reducing electron-transfer enzymes[1–3], is located at the University of Helsinki (Helsinki, Finland) where measurements were performed. A pulsed 150-W xenon arc lamp (Applied Photophysics, Surrey, U.K.) was used as the probe light source. After passing through the sample, the probe light was directed using a fiber optic cable (300 μm, UV-VIS XSR solarization-resistant, Ocean Optics, Dunedin, FL) to either of the two detectors incorporated into one setup. A Triax-180 compact imaging spectrometer (HORIBA Jobin Yvon, Edison, NJ) delivers spectral imaging over a fast kinetic CCD matrix (DV420-UV-FK; Andor Technology, Belfast City, Ireland) to allow recording absorption change surfaces with time resolution of 1–16 μs between the spectra. The slower reaction on a time scale from tens of microseconds to minutes was measured with an in-house-built spectrometer based on Sprint spL 2,048–140 km linear scan camera (Basler vision technologies, time resolution, 12 μs between the spectra). The wavelength-time-absorption data surfaces from these two detectors were combined into a single surface containing the absorbance changes developed after the laser flash. The setup was operated by software written by Nikolai Belevich (University of Helsinki, Helsinki, Finland).

Photolysis of the proteins were achieved with single-flash laser excitation at 532 nm (maximum intensity, 340 mW/cm^2, 50 mm^2 spot area, 4 ns per pulse) provided by a 2nd harmonic generator attached to a Q-switched Nd-YAG laser (Brilliant B, Quantel, Les Ulis, France). The laser beam was focused, using a pair of cylindrical quartz lenses, on the larger side of a quartz fluorescence microcuvette (10 $\times$ 2 mm optical path, Hellma Analytics, Müllheim, Germany) and covered 10 $\times$ 2 mm area of the sample. The laser-illuminated spot was slightly larger than the sample area exposed to the probe light, lessening the possibility of slow, diffusion-related artifacts. Each data surface was an average of 10-25 laser flashes. Fresh, dark-adapted sample (OD595 = 1.0 for KillerRed and mRFP, OD560 = 1.0 for DsRed) was taken every time for the flash excitation during averaging, so that each sample was illuminated only once. The sample was exposed to the probe light ~0.5 ms prior to the flash excitation using a mechanical shutter (Uniblitz LS2, 2 mm aperture, 300 μs

opening time, Vincent Associates, Rochester, NY) to minimize the actinic effect of the white light. All measurements were performed at ambient temperature.

The wavelength-time-absorption surfaces of TA changes in the 1 μs – 1 min time window following the photolysis were decomposed into a multiexponential decay function using a global fit algorithm:

$$\Delta A(t, \lambda) = \sum_i \varepsilon_i(\lambda) \exp\left(-t/\tau_i\right) \tag{1}$$

where $\Delta A(t, \lambda)$ is the optical absorption change at time t ($t = 0$ at the instance of laser flash) and at wavelength λ, and $\epsilon_i(\lambda)$ and τ_i are the characteristic spectrum and time constant for the i-th exponential decay component, respectively. All data treatment was performed in MATLAB (version 7.8, MathWorks, Natick, MA).

E.   Anaerobic/aerobic measurements

Anaerobic samples were prepared using a gas/vacuum line of local design. A 4×10×30 mm fluorescence quartz cell was sealed to a Kimble-Kontes high-vacuum stopcock, which had a vacuum O-ring connection to the vacuum line. As a typical degassing procedure, 20 cycles of exchanging vacuum (10^{-6} bar) and pure Ar were followed by shaking the cell filled with Ar for 15 min on an orbital shaker; then the procedure was repeated 2 more times. 99.99% Ar was additionally purified using the Agilent Technologies BOT-2 and IOT oxygen scrubbers. Aerobic samples were bubbled with oxygen for 10 minutes before TA measurements.

II.   RESULTS

A.   Time-correlated single photon counting measurements

Fig. S1 shows fluorescence decay of RFPs using 467 and 590 nm excitation. The first laser has a 60 ps pulse width, but hits at the blue edge of absorption band of the red chromophore, and at the absorption bands of non-matured or decomposed product (see Fig. S6). So, it resulted in dual emission, but the red emission peak (590-620 nm) was still dominating. 590 nm LED has 10 times wider excitation peak, but hits very close to the absorption maxima of KillerRed and mRFP, or the red edge of the DsRed. It is important, that the fluorescence lifetimes determined using both excitation sources (Fig. S1) were the same within experimental error. The fluorescence lifetimes

of KillerRed, mRFP, and DsRed were 1.6, 2.0, and 3.6 ns respectively. The latter value matches the published value[4].
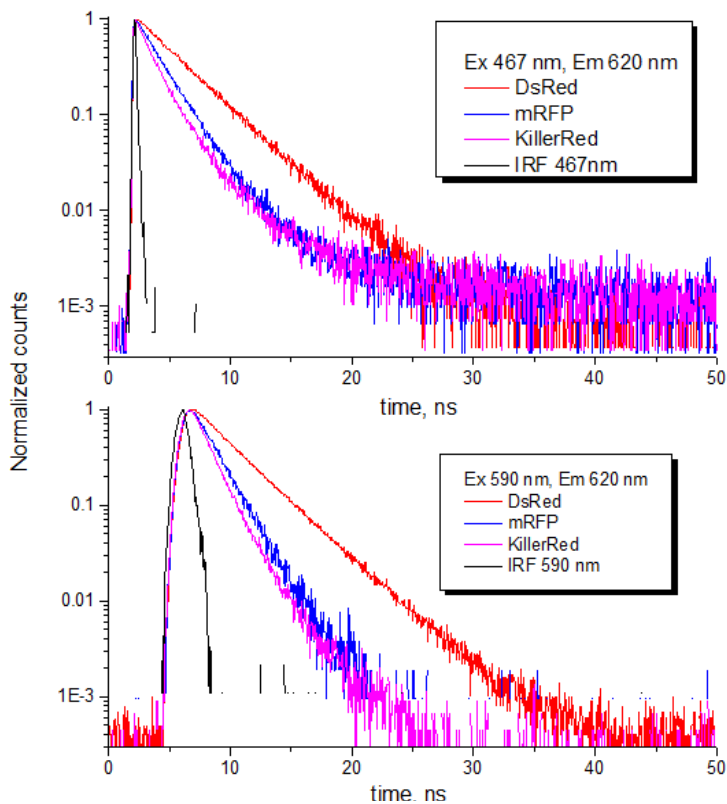

FIG. S1: Fluorescence decay curves of RFPs under 467 nm (top) and 590 nm (bottom) pulsed excitation.

B. Transient absorption spectroscopy measurements (picosecond-to-nanosecond time domain)

Fig. S2 shows sub-picosecond decay of transient absorption of KillerRed. Analysis of the ps-ns TA spectra of KillerRed is presented in the main text. Here we add that TA ps-ns spectra of all RFPs were almost identical and differ by the decay lifetimes of the S_1 absorptions bands.

C. Transient absorption spectroscopy measurements (μs-to-second time domain)

The TA spectra of the three RFPs in μs to ms range are shown in Fig. 2 of the main manuscript. The main spectral features and the respective lifetimes are summarized in Table 1 of the main manuscript. Fig. S3 shows the results of multi-exponential fit of the TA spectra. The last time
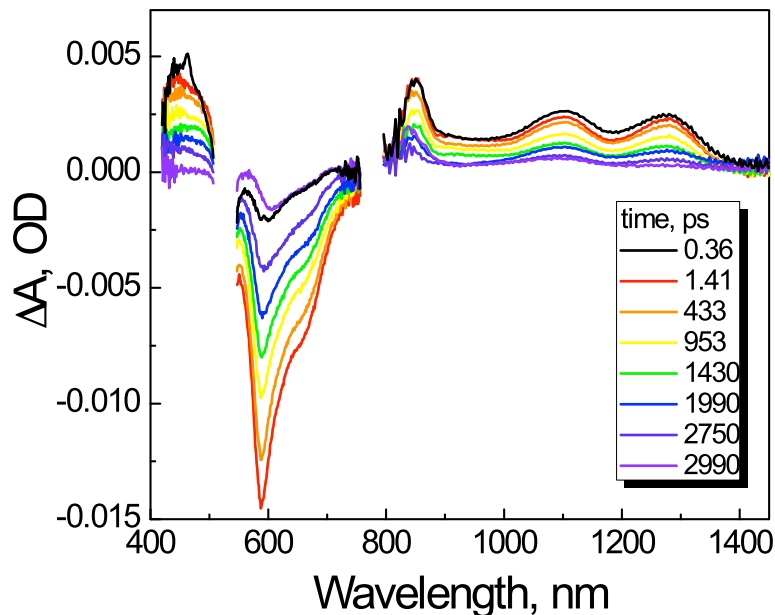
FIG. S2: Sub-picosecond decay of transient absorption of KillerRed at pH 7.5 upon excitation with 100 fs 532 nm (2.33 eV) laser pulse. For the experimental conditions, see Section I.

point (4 seconds) has absorption at 576 nm (2.15 eV), which can be attributed to the production of decaboxylated photoproduct[5] (Fig. S3).

D. Quenching experiments

The effects of several oxidants and reductants (cytochrome C, β-mercaptoethanol, NAD^+, potassium ferricyanide, flavin mononucleotide) were tested on the kinetics of the main transient component in KillerRed, mRFP, and DsRed. Each oxidant or reductant was added to the protein solution in μM concentrations before acquiring the TA. In all three cases, the kinetics were unaffected by the additional of these agents. The oxidants and reductants are mostly likely too large and therefore are unable to access the chromophore environment in each of the proteins. Therefore, we tested a smaller molecule, H_2O_2. Aliquots of H_2O_2 were added to the protein solution within 30 seconds of each measurement. Each data surface was an average of 5-10 laser flashes and fresh protein was used for each flash. Hydrogen peroxide had little to no effect on steady state absorption of the proteins, as illustrated in Fig. S4). The lifetimes of the RFPs in the presence of H_2O_2 were affected in the order of DsRed > mRFP > KillerRed (Fig. S5).

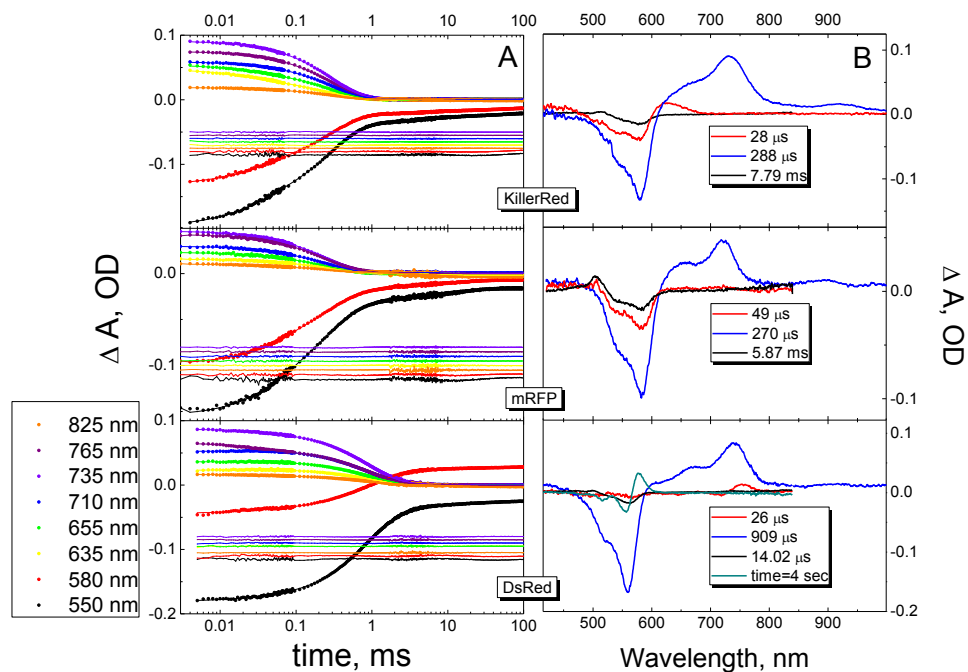FIG. S3: The results of the multiexponential fit for KillerRed (top), mRFP (middle), and DsRed (bottom).
(A) The data transients at selected wavelengths, the fit results, and the RMS residuals are shown. (B) The
spectra of the respective kinetic components are shown. Time constants are indicated.
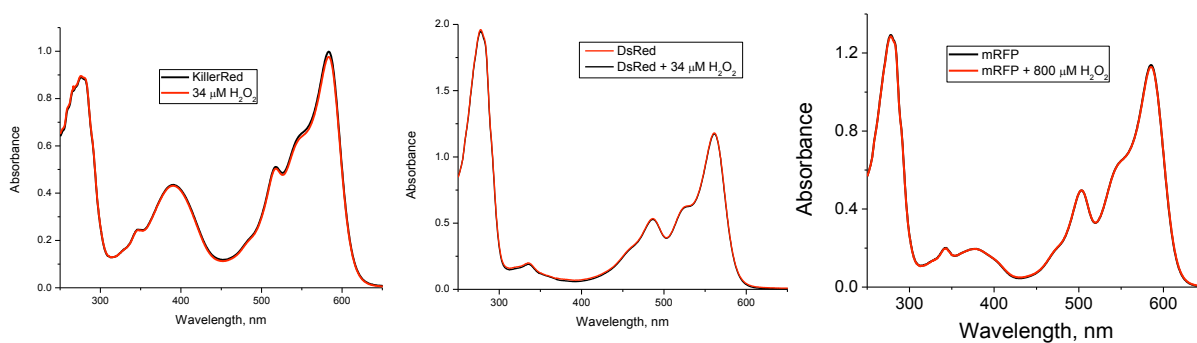

FIG. S4: Absorbance of KillerRed (left), DsRed (middle), and mRFP (right) at ambient conditions and in
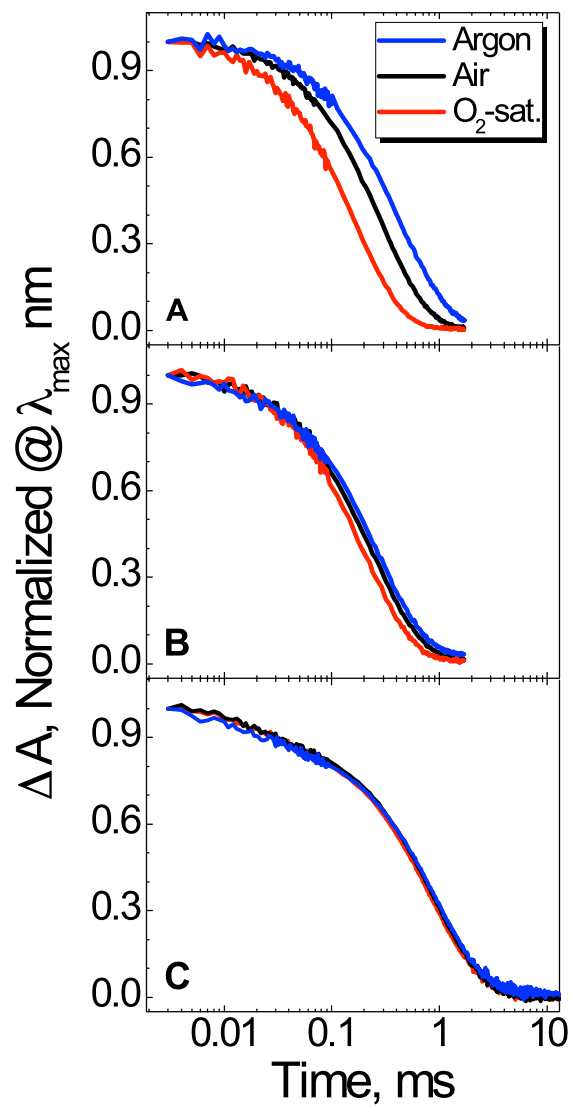the presence of H_2O_2.

FIG. S5: Kinetics of the RSI in KillerRed (top), mRFP (middle), and DsRed (bottom) for aerobic (standard) sample, fully anaerobic, and oxygen-saturated conditions.

E. Bleaching and power dependence

Fig. S6 shows absorption spectra of the three proteins measured following increased irradiation by 532 nm laser. Consistently with the previously published work, increased exposure results in a graduate decrease in absorbance, due to bleaching of the sample. Importantly, the degree of bleaching is insignificant on the scale of our TA experiments.
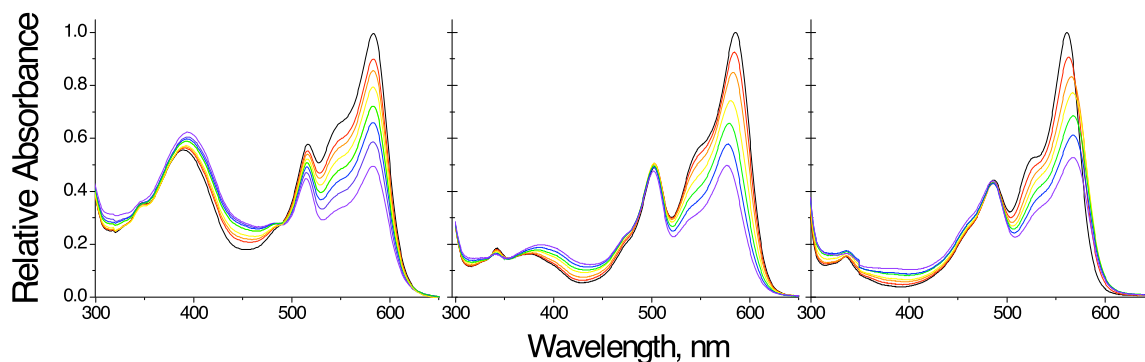

FIG. S6: Irradiation of KillerRed (left), mRFP (middle), and DsRed (right) with 532 nm pulsed laser.

Fig. S7 compares the TA of bleached DsRed versus that of fresh DsRed. Bleaching of DsRed results in a red shifted photoproduct. Based on the work by Habuchi and coworkers[5], we attribute this red-shifted photoproduct to the trans anionic chromophore. Upon converting the majority of fresh DsRed to bleached photoproduct, we were able to excite this photoproduct (the trans anion) and still see this photoreduction of this form, too. Most importantly, if one looks at the TA decay for bleached DsRed (Fig. S7), little to no rise at 580 nm is seen, which demonstrates that it is mostly the photoproduct that is excited. We note that the lifetime of the transient in bleached DsRed is significantly longer that of fresh protein.

The power dependence of the transient signal of the RFPs (532 nm excitation) was performed using neutral density filters. Figure S8 shows the TA signal at different flash energies at 16 μs. The power dependence is hyperbolic, which is characteristic of one-photon absorption. The hyperbolic dependence is due to long pulse-width (4 ns) used in our experiments.
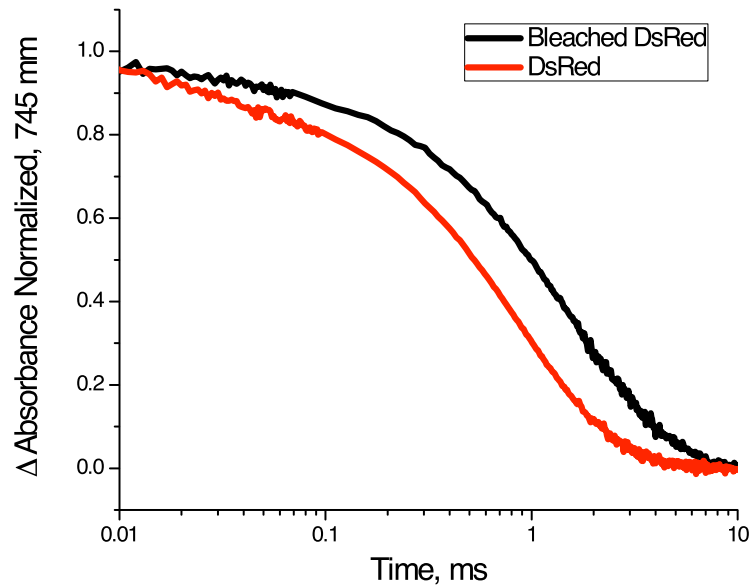
FIG. S7: Decay of the TA signal in fresh and bleached DsRed.
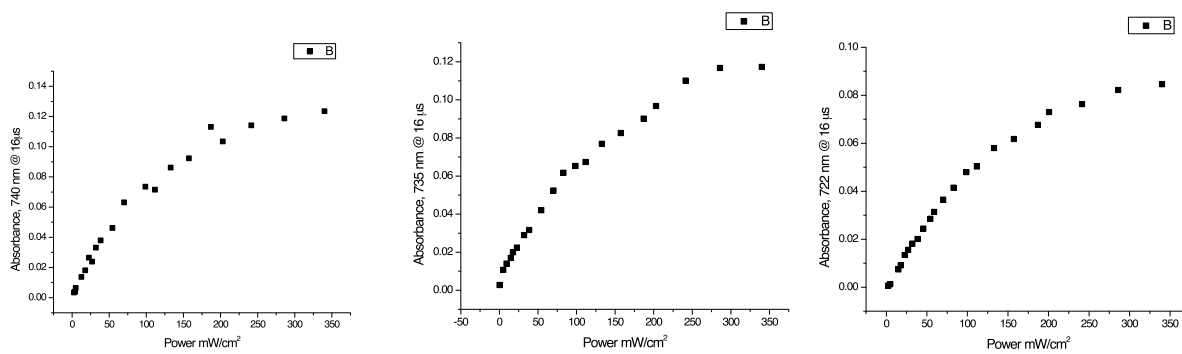

FIG. S8: Power dependence of the transient absorption signal at 16 μs in KillerRed (left), mRFP (middle), and DsRed (right).
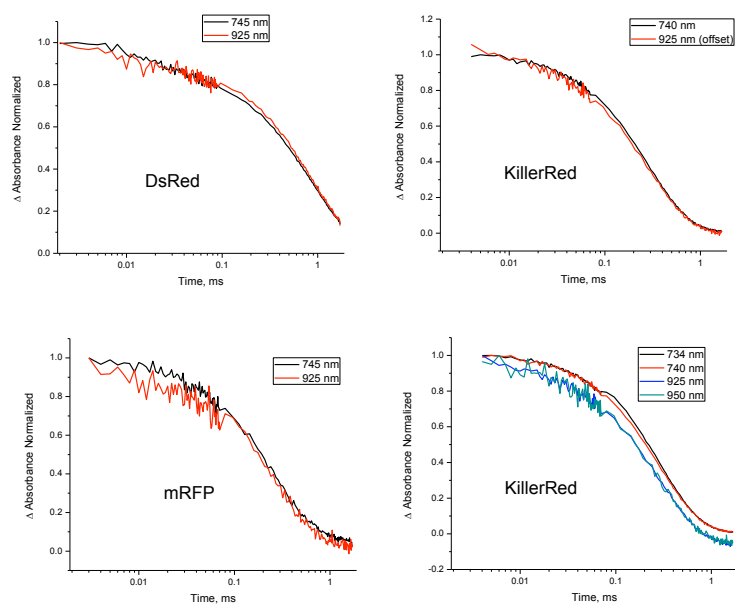
FIG. S9: Kinetics of the signal decay at 740 and 925 nm. The data confirm that the two bands are likely to be due to absorption by the same species.

III.   COMPUTATIONAL DETAILS

Excitation energies of the anionic chromophore were computed using scaled opposite spin technique applied to perturbative doubles corrected configuration interaction singles, SOS-CIS(D) (Ref. [6]). Excitation energies of the radical species (neutral radical and dianion-radical) were computed by TDDFT with the B5050LYP functional (equal mixture of 50% HF +8% Slater + 42% Becke for exchange and 19% VWN + 81% LYP for correlation [7]). Electron attachment and detachment energies were computed with ωB97X-D (Ref. [8, 9]). The 6-31G(d,p) basis[10] was used for excitation energies calculations. The cc-pVDZ basis[11] was employed for attachment/detachment energies calculations. In addition, extrapolation to the aug-cc-pVTZ values[11] was performed using calculations at selected snapshots, as described below.

A.   Protonation state of Glu68 and Glu218

Carboxylates of both of Glu68 and Glu218 were considered to be protonated based on the results of PROPKA predictions (estimated pKa > 8) and based on the analysis of the possible H-bonding patterns in X-ray structure. The distance between Glu218 carboxylate oxygen and the chromophore nitrogen is only 3.0 Å, which supports protonated form. The possible H-bond network for Glu68 is shown in Fig. S10. The proposed H-bonding pattern is also consistent with the protonated form of Glu68.
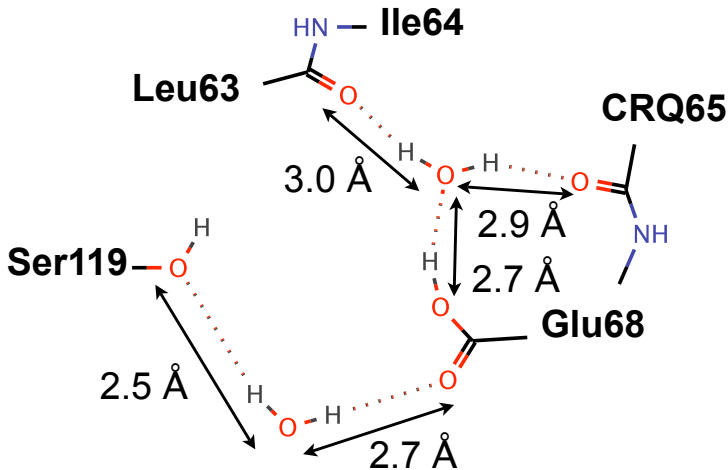
FIG. S10: Chromophore atoms included in the QM part.

B.   QM/MM setup
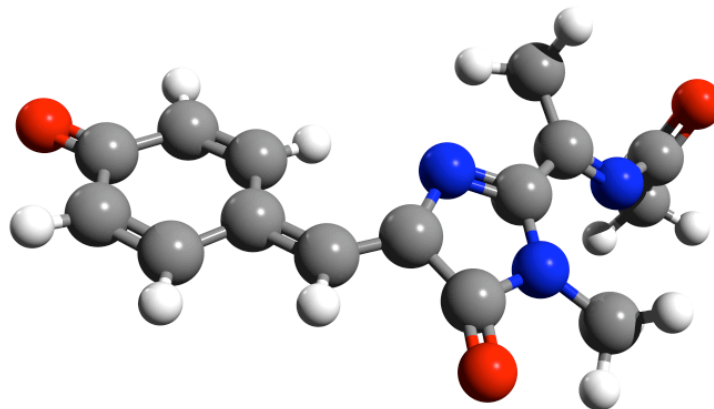
FIG. S11: Chromophore atoms included in the QM part.

Arg94 is the only charged residue directly hydrogen bonded to the chromophore. Thus, one may anticipate that among all other neighboring residues, Arg94 could lead to the strongest shift in computed excitation energies if included in the QM part. Table S1 lists computed excitation energies for several representative computational setups. The quantum part either included the chromophore or the chromophore and Arg94 side chain. The MM part consisted of either Arg94 or the entire protein molecule (with Arg94 point charges excluded if the residue is in QM). The geometries are taken from the t=0 snapshot of the production run MD trajectory. As follows from comparison of lines 1,2, and 3, the point charge model accurately represents the effect of Arg94 side chain (Δ=0.04 eV). This is also consistent with only 0.07 eV difference between QM(Chro)/MM and QM(Chro+Arg94)/MM calculations (lines 4 and 5).

TABLE S1: SOS-CIS(D)/6-31G(d,p) excitation energies (eV) computed for several cluster and QM/MM models.

QM	MM	ΔE, eV
Chro	–	2.24
Chro	Arg94	2.57
Chro +Arg94	–	2.61
Chro+Arg94	All	2.44
Chro	All	2.51

C.   Basis set effects

TABLE S2: Methods used to compute excitation, electron detachment, and electron attachment energies along MD trajectory. The snapshots were extracted each 20 ps.

Quantity	Method (QM)
VEE (^{1}Chro$^-$ →^{1}Chro^{-*})	SOS-CIS(D)/6-31G(d,p)
VEA (^{1}Chro$^-$ →^{2}Chro^{2-})	ωB97X-D/cc-pVDZ
VDE (^{1}Chro$^-$ →^{2}Chro^0)	ωB97X-D/cc-pVDZ
VEE (^{2}Chro^{2-} →^{2}Chro^{2-*})	TDDFT(B5050LYP)/6-31G(d,p)
VEE (^{2}Chro^0 →^{2}Chro^{0*})	TDDFT(B5050LYP)/6-31G(d,p)
ST gap (^{1}Chro$^-$ →^{3}Chro$^-$)	SOS-CIS(D)/6-31G(d,p)
VEE (^{3}Chro$^-$ →^{3}Chro^{-*})	SOS-CIS(D)/6-31G(d,p)

To quantify the effects of the basis set extension (to aug-cc-pVTZ), energy calculations were performed for several snapshots along the MD trajectory (each 200 ps). As follows from the data shown below (Tables S3–S8), the shifts due to the basis set extension are almost constant for different geometries. Thus, we used the resulting shifts to extrapolate values computed at each 20 ps to the aug-cc-pVTZ basis. The extrapolated trajectories are shown in Fig. 3 and Fig. S12.

TABLE S3:   QM:SOS-CIS(D)/MM:CHARMM27 excitation energies of the KillerRed protein. ^{1}Chro$^-$ →^{1}Chro^{-*} excitation energies for different bases are shown, eV. Δ is the difference in excitation energy computed with the 6-31G(d,p) and aug-cc-pVTZ basis sets.

Basis set	Time, ps				
	0	200	400	600	800
6-31G(d,p)	2.51	2.48	2.40	2.43	2.38
6-31+G(d,p)	2.45	2.42	2.33	2.34	2.36
6-311+G(d,p)	2.43	2.39	2.31	2.33	2.29
aug-cc-pVDZ	2.43	2.39	2.31	2.32	2.28
aug-cc-pVTZ	2.37	2.33	2.25	2.26	2.23
Δ		-0.14	-0.15	-0.15	-0.17	-0.15
$\bar{\Delta}$			-0.15		

TABLE S4: QM:SOS-CIS(D)/MM:CHARMM27 ^{1}Chro$^-$–^{3}Chro$^-$ gap and ^{3}Chro$^-$ →^{3}Chro^{-*} excitation energies.

time, ps	^{1}Chro$^-$–^{3}Chro$^-$, eV			^{3}Chro$^-$ →^{3}Chro^{-*}, eV		
	6-31G(d,p)	aug-cc-pVTZ	Δ	6-31G(d,p)	aug-cc-pVTZ	Δ
200	1.82	1.74	-0.08	1.23	1.26	0.03
400	1.77	1.69	-0.08	1.27	1.30	0.03
600	1.82	1.73	-0.08	1.21	1.26	0.05
800	1.78	1.69	-0.09	1.33	1.36	0.03
$\bar{\Delta}$			-0.09			0.04

TABLE S5: QM:ωB97X-D/MM:CHARMM27 ^{1}Chro$^-$ →^{2}Chro^{2-} electron affinities.

time, ps	^{1}Chro$^-$ →^{2}Chro^{2-}, eV			
	cc-pVDZ	aug-cc-pVDZ	aug-cc-pVTZ	Δ
0	1.43	1.87	1.87	0.44
200	1.47	1.91	1.91	0.44
600	0.98	1.45	1.45	0.47
800	1.19	1.63	1.63	0.44
$\bar{\Delta}$				0.44

TABLE S6: QM/MM:CHARMM27 ^{2}Chro^{2-} →^{2}Chro^{2-*} excitation energies.

time, ps	^{2}Chro^{2-} →^{2}Chro^{2-*}, eV			
	50:50			ωB97X-D
	6-31G(d,p)	aug-cc-pVTZ	Δ	6-31G(d,p)
0	1.69	1.63	-0.06	1.63
200	1.71	1.65	-0.06	1.65
400	1.77	1.73	-0.04	1.69
600	1.76	1.69	-0.07	1.70
800	1.79	1.74	-0.05	1.73
$\bar{\Delta}$			-0.06	

TABLE S7: QM/MM:CHARMM27 ^{1}Chro$^-$ $\to^2$Chro^0 vertical detachment energies.

	^{1}Chro$^-$ $\to^2$Chro^0, eV			
time, ps	50:50		ωB97X-D	
	aug-cc-pVTZ	cc-pVDZ	aug-cc-pVTZ	Δ
0	7.18	6.96	7.28	0.32
200	7.08	6.87	7.20	0.33
400	7.22	6.99	7.32	0.33
600	6.66	6.41	6.76	0.35
800	6.83	6.57	6.88	0.31
$\bar{\Delta}$				0.33

TABLE S8: QM:50:50/MM:CHARMM27 ^{2}Chro^0 $\to^2$Chro^{0*} excitation energies.

	^{2}Chro^0 $\to^2$Chro^{0*}, eV		
time, ps	6-31G(d,p)	aug-cc-pVTZ	Δ
0	2.22	2.30	0.09
200	2.02	2.11	0.09
$\bar{\Delta}$			0.09

TABLE S9: Lowest excitation energies of ^{2}Chro^0 computed with SOS-CIS(D)/6-31G(d,p). ROHF reference was used.

State	ΔE, eV	f_L
1	2.16	6×10^{-2}
2	3.00	7×10^{-3}
3	3.39	1.4
4	3.60	9×10^{-2}
5	3.71	1×10^{-3}

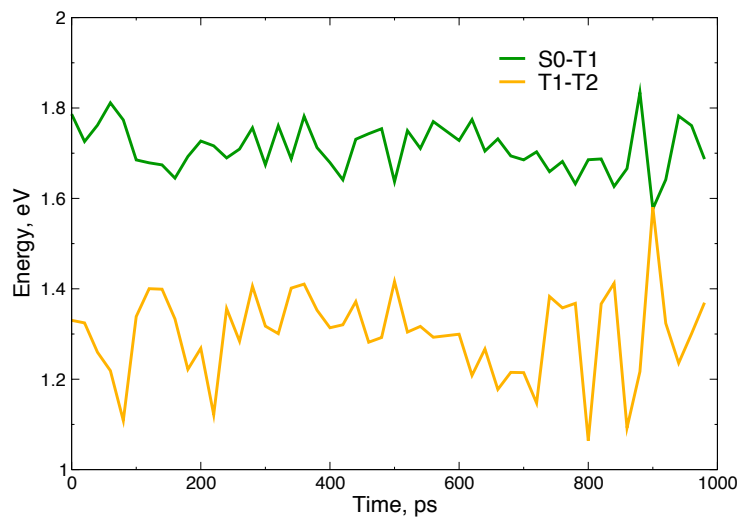**D.   Triplet states of KillerRed**

FIG. S12: Fluctuations of the singlet-triplet gap (S_0–T_1) and energy difference between the two lowest triplets (T_1–T_2) along the MD trajectory.

[1] Belevich, I.; Gorbikova, E.; Belevich, N.P.; Rauhamäki, V.; Wikström, M.; Verkhovsky, M.I. Initiation of the proton pump of cytochrome c oxidase *Proc. Nat. Acad. Sci.* **2010**, *107*, 18469–18474.

[2] Borisov, V.B.; Belevich, I.; Bloch, D.A.; Mogi, T.; Verkhovsky, M.I. Glutamate 107 in subunit i of cytochrome bd from Escherichia coli is part of a transmembrane intraprotein pathway conducting protons from the cytoplasm to the heme b(595)/heme d active site *Biochem.* **2008**, *47*, 7907–7914.

[3] Belevich, I.; Bloch, D.A.; Belevich, N.; Wikström, M.; Verkhovsky, M.I. Exploring the proton pump mechanism of cytochrome c oxidase in real time *Proc. Nat. Acad. Sci.* **2007**, *104*, 2685–2690.

[4] Heikal, A.A.; Hess, S.T.; Baird, G.S.; Tsien, R.Y.; Webb, W.W. Molecular spectroscopy and dynamics of intrinsically fluorescent proteins: Coral red (dsRed) and yellow (Citrine) *Proc. Nat. Acad. Sci.* **2000**, *97*, 11996–12001.

[5] Habuchi, S.; Cotlet, M.; Gensch, T.; Bednarz, T.; Haber-Pohlmeier, S.; Rozenski, J.; Dirix, G.; Michiels, J.; Vanderleyden, J.; Heberle, J.; Schryver, F.C. De; Hofkens, J. Evidence for the isomerization and decarboxylation in the photoconversion of the red fluorescent protein dsred *J. Am. Chem. Soc.* **2005**, *127*, 8977–8984.

[6] Rhee, Y.M.; Head-Gordon, M. Scaled second order perturbation corrections to configuration interaction singles: efficient and reliable excitation energy methods *J. Phys. Chem. A* **2007**, *111*, 5314–5326.

[7] Shao, Y.; Head-Gordon, M.; Krylov, A.I. The spin-flip approach within time-dependent density functional theory: Theory and applications to diradicals *J. Chem. Phys.* **2003**, *118*, 4807–4818.

[8] Chai, J.-D.; Head-Gordon, M. Systematic optimization of long-range corrected hybrid density functionals *J. Chem. Phys.* **2008**, *128*, 084106.

[9] Chai, J.-D.; Head-Gordon, M. Long-range corrected hybrid density functionals with damped atom-atom dispersion interactions *Phys. Chem. Chem. Phys.* **2008**, *10*, 6615–6620.

[10] Hehre, W.J.; Ditchfield, R.; Pople, J.A. Self-consistent molecular orbital methods. XII. Further extensions of gaussian-type basis sets for use in molecular orbital studies of organic molecules *J. Chem. Phys.* **1972**, *56*, 2257.

[11] Dunning, T.H. Gaussian basis sets for use in correlated molecular calculations. I. The atoms boron through neon and hydrogen *J. Chem. Phys.* **1989**, *90*, 1007–1023.

CRQ Parameters

Charges

Atom	Charge (e)
C3	0.61
O3	-0.61
N	-0.371
CA1	0.372
CB1	-0.516
HB11	0.27
HB12	0.27
CG1	-0.571
HG1	0.243
HG2	0.243
C1	0.348
N2	-0.454
N3	-0.493
C2	0.665
O2	-0.662
CA2	-0.092
CA3	-0.324
HA1	0.267
HA2	0.274
CB2	-0.049
HB11	0.252
CG2	-0.201
CD1	-0.184
HD1	0.221
CD2	-0.19
HD2	0.25
CE1	-0.331
HE1	0.234
CE2	-0.308
HE2	0.237
CZ	0.375
OH	-0.789
OE1	-0.657
C	0.604
O	-0.6
CD3	0.692
NE1	-0.874
HE31	0.43
HE32	0.419

Bond Lengths and Force Constants

Bond	Length Angstrom	Force Constant kcal/(mol*A^2)
C3-O3	1.222	529.5
C3-N	1.383	457.0
N-CA1	1.291	483.0
CA1-CB1	1.509	250.0
CA1-C1	1.452	469.0
CB1-HB11	1.090	322.0
CB1-HB12	1.090	322.0
CB1-CG1	1.530	222.5
CG1-HG1	1.111	309.0
CG1-HG2	1.111	309.0
CG1-CD3	1.522	200.0
C1-N2	1.314	400.0
C1-N3	1.390	400.0
N2-CA2	1.373	400.0
N3-C2	1.398	400.0
N3-CA3	1.445	250.0
C2-O2	1.236	854.0
C2-CA2	1.455	410.0
CA2-CB2	1.398	435.8
CA3-HA1	1.111	309.0
CA3-HA3	1.111	309.0
CA3-C	1.490	250.0
CB2-HB	1.091	360.5
CB2-CG2	1.393	447.8
CG2-CD1	1.437	303.8
CG2-CD2	1.438	303.8
CD1-HD1	1.089	340.0
CD1-CE1	1.360	307.4
CD2-HD2	1.085	340.0
CD2-CE2	1.360	307.4
CE1-HE1	1.086	340.0
CE1-CZ	1.459	303.8
CE2-HE2	1.087	340.0
CE2-CZ	1.462	303.8
CZ-OH	1.245	842.0
OE1-CD3	1.230	650.0
C-O	1.230	650.0
CD3-NE1	1.360	430.0
NE1-HE31	1.000	480.0
NE1-NE32	1.000	480.0

Appendix

Bond Angles and Force Constants

Bonds	Angle Degrees	Force Constant kcal/(mol*Rad^2)
CA4-C3-O3	122.2	80.00
CA4-C3-N	113.8	80.00
O3-C3-N	123.9	80.00
C3-N-CA1	123.3	33.40
N-CA1-CB1	124.1	80.00
N-CA1-C1	119.8	70.00
CB1-CA1-C1	116.1	52.00
CA1-CB1-HB11	109.5	33.00
CA1-CB1-HB12	109.5	33.00
CA1-CB1-CG1	109.5	33.00
HB11-CB1-HB12	109.0	35.50
HB11-CB1-CG1	110.1	26.50
HB12-CB1-CG1	110.1	26.50
CB1-CG1-HG1	110.1	26.50
CB1-CG1-HG2	110.1	26.50
CB1-CG1-CD3	108.0	52.00
HG1-CG1-HG2	109.0	35.50
HG1-CG1-CD3	109.5	38.00
HG2-CG1-CD3	109.5	38.00
CA1-C1-N2	122.0	40.00
CA1-C1-N3	125.8	40.00
N2-C1-N3	112.3	130.00
C1-N2-CA2	106.8	130.00
C1-N3-C2	107.7	130.00
C1-N3-CA3	130.3	40.00
C2-N3-CA3	121.9	40.00
N3-C2-O2	124.6	50.00
N3-C2-CA2	103.3	130.00
O2-C2-CA2	132.1	44.00
N2-CA2-C2	109.9	130.00
N2-CA2-CB2	127.1	45.80
C2-CA2-CB2	123.0	45.80
N3-CA3-HA1	109.5	38.00
N3-CA3-HA2	109.5	38.00
N3-CA3-C	108.0	52.00
HA1-CA3-HA2	109.0	35.50
HA1-CA3-C	109.5	33.00
HA2-CA3-C	109.5	33.00
CA2-CB2-HB	112.5	42.00
CA2-CB2-CG2	131.5	130.00
HB-CB2-CG2	116.0	42.00
CB2-CG2-CD1	118.8	45.80
CB2-CG2-CD2	124.6	45.80
CD1-CG2-CD2	116.6	40.00
CG2-CD1-HD1	117.6	30.00
CG2-CD1-CE1	122.6	40.00
HD1-CD1-CE1	119.9	30.00
CG2-CD2-HD2	117.7	30.00
CG2-CD2-CE2	121.7	40.00

Bond Angles and Force Constants (Cont.)

Bonds	Angle Degrees	Force Constant kcal/(mol*Rad^2)
HD2-CD2-CE2	120.7	30.00
CD1-CE1-HE1	121.5	30.00
CD1-CE1-CZ	121.6	40.00
HE1-CE1-CZ	116.9	30.00
CD2-CE2-HE2	121.4	30.00
CD2-CE2-CZ	122.4	40.00
HE2-CE2-CZ	116.3	30.00
CE1-CZ-CE2	115.3	40.00
CE1-CZ-OH	122.5	45.20
CE2-CZ-OH	122.3	45.20
CA3-C-O	121.0	15.00
CA3-C-N4	116.5	80.00
O-C-N4	122.5	80.00
CG1-CD3-OE1	121.0	15.00
CG1-CD3-NE1	116.5	50.00
OE1-CD3-NE1	122.5	75.00
CD3-NE1-HE31	120.0	50.00
CD3-NE1-HE32	120.0	50.00
HE31-NE1-HE32	120.0	23.00
C-N(GLU)-NH(GLU)	123.0	34.00
C-N(GLU)-CA(GLU)	120.0	50.00

Dihedral Angles and Force Constants

Atoms	Angle Degress	Force Constant kcal/mol	
CA4-C3-N-CA1	180	1.54	2
O3-C3-N-CA1	180	1.54	2
C3-N-CA1-CB1	180	1.71	2
C3-N-CA1-C1	180	1.71	2
N-CA1-CB1-HB11	180	0.00	3
N-CA1-CB1-HB12	180	0.00	3
N-CA1-CB1-CG1	180	1.40	1
C1-CA1-CB1-HB11	0	0.00	3
C1-CA1-CB1-HB12	0	0.00	3
C1-CA1-CB1-CG1	0	1.40	1
N-CA1-C1-N2	180	3.99	2
N-CA1-C1-N3	180	3.99	2
CB1-CA1-C1-N2	180	1.60	2
CB1-CA1-C1-N3	180	1.60	2
CA1-CB1-CG1-HG1	0	0.20	3
CA1-CB1-CG1-HG2	0	0.20	3
CA1-CB1-CG1-CD3	0	0.20	3
HB11-CB1-CG1-HG1	0	0.20	3
HB11-CB1-CG1-HG2	0	0.20	3
HB11-CB1-CG1-CD3	0	0.20	3
HB12-CB1-CG1-HG1	0	0.20	3
HB12-CB1-CG1-HG2	0	0.20	3
HB12-CB1-CG1-CD3	0	0.20	3
CB1-CG1-CD3-OE1	0	1.40	1
CB1-CG1-CD3-NE1	0	0.00	1
HG1-CG1-CD3-OE1	180	0.00	2
HG1-CG1-CD3-NE1	180	0.00	2
HG2-CG1-CD3-OE1	180	0.00	2
HG2-CG1-CD3-NE1	180	0.00	2
CA1-C1-N2-CA2	180	14.00	2
N3-C1-N2-CA2	180	14.00	2
CA1-C1-N3-C2	180	14.00	2
CA1-C1-N3-CA3	180	9.22	2
N2-C1-N3-C2	180	14.00	2
N2-C1-N3-CA3	180	9.22	2
C1-N2-CA2-C2	180	14.00	2
C1-N2-CA2-CB2	180	9.22	2
C1-N3-C2-O2	180	11.61	2
C1-N3-C2-CA2	180	14.00	2
CA3-N3-C2-O2	180	9.22	2
CA3-N3-C2-CA2	180	9.22	2
C1-N3-CA3-HA1	180	0.20	3
C1-N3-CA3-HA2	180	0.20	3
C1-N3-CA3-C	180	0.20	3
C2-N3-CA3-HA1	0	0.20	3
C2-N3-CA3-HA2	0	0.20	3
C2-N3-CA3-C	0	0.20	3
N3-C2-CA2-N2	180	14.00	2
N3-C2-CA2-CB2	180	11.61	2

Dihedral Angles and Force Constants (Cont.)

Atoms	Angle Degress	Force Constant kcal/mol	
O2-C2-CA2-N2	180	11.61	2
O2-C2-CA2-CB2	180	7.79	2
N2-CA2-CB2-HB	180	3.90	2
N2-CA2-CB2-CG2	180	3.90	2
C2-CA2-CB2-HB	180	3.90	2
C2-CA2-CB2-CG2	180	3.90	2
CA2-CB2-CG2-CD1	180	2.70	2
CA2-CB2-CG2-CD2	180	2.70	2
HB-CB2-CG2-CD1	180	2.70	2
HB-CB2-CG2-CD2	180	2.70	2
CB2-CG2-CD1-HD1	180	2.40	2
CB2-CG2-CD1-CE1	180	3.10	2
CD2-CG2-CD1-HD1	180	3.50	2
CD2-CG2-CD1-CE1	180	3.10	2
CB2-CG2-CD2-HD2	180	2.40	2
CB2-CG2-CD2-CE2	180	3.10	2
CD1-CG2-CD2-HD2	180	3.50	2
CD1-CG2-CD2-CE2	180	3.10	2
CG2-CD1-CE1-HE1	180	3.50	2
CG2-CD1-CE1-CZ	180	3.10	2
HD1-CD1-CE1-HE1	180	2.40	2
HD1-CD1-CE1-CZ	180	3.50	2
CG2-CD2-CE2-HE2	180	3.50	2
CG2-CD2-CE2-CZ	180	3.10	2
HD2-CD2-CE2-HE2	180	2.40	2
HD2-CD2-CE2-CZ	180	3.50	2
CD1-CE1-CZ-CE2	180	3.10	2
CD1-CE1-CZ-OH	180	3.10	2
HE1-CE1-CZ-CE2	180	3.50	2
HE1-CE1-CZ-OH	180	4.20	2
CD2-CE2-CZ-CE1	180	3.10	2
CD2-CE2-CZ-OH	180	3.10	2
HE2-CE2-CZ-CE1	180	3.50	2
HE2-CE2-CZ-OH	180	4.20	2